

Spitzer + VLTI-GRAVITY Measure the Lens Mass of a Nearby Microlensing Event

WEICHENG ZANG,¹ SUBO DONG,² ANDREW GOULD,^{3,4} SEBASTIANO CALCHI NOVATI,⁵ PING CHEN,^{2,6} HONGJING YANG,¹
SHUN-SHENG LI,^{7,8} SHUDE MAO,^{1,7} K.B. ALTON,⁹ J. BRIMACOMBE,¹⁰ SEAN CAREY,¹¹ G. W. CHRISTIE,¹²
F. DELPLANCKE-STRÖBELE,¹³ DAX L. FELIZ,¹⁴ J. GREEN,¹⁵ SHAOMING HU,¹⁶ T. JAYASINGHE,^{17,18} R. A. KOFF,¹⁹ A. KURTENKOV,²⁰
A. MÉRAND,¹³ MILEN MINEV,²¹ ROBERT MUTEL,²² T. NATUSCH,²³ TYLER ROTH,²² YOSHI SHVARTZVALD,²⁴ FENGWU SUN,²⁵
T. VANMUNSTER,²⁶ AND WEI ZHU²⁷

¹*Department of Astronomy and Tsinghua Centre for Astrophysics, Tsinghua University, Beijing 100084, China*

²*Kavli Institute for Astronomy and Astrophysics, Peking University, Yi He Yuan Road 5, Hai Dian District, Beijing 100871, China*

³*Max-Planck-Institute for Astronomy, Königstuhl 17, 69117 Heidelberg, Germany*

⁴*Department of Astronomy, Ohio State University, 140 W. 18th Ave., Columbus, OH 43210, USA*

⁵*IPAC, Mail Code 100-22, Caltech, 1200 E. California Blvd., Pasadena, CA 91125, USA*

⁶*Department of Astronomy, School of Physics, Peking University, Yi He Yuan Road 5, Hai Dian District, Beijing 100871, China*

⁷*National Astronomical Observatories, Chinese Academy of Sciences, Beijing 100101, China*

⁸*School of Astronomy and Space Science, University of Chinese Academy of Sciences, Beijing 100049, China*

⁹*Desert Blooms Observatory*

¹⁰*Coral Towers Observatory, Cairns, Queensland 4870, Australia*

¹¹*Spitzer Science Center, MS 220-6, California Institute of Technology, Pasadena, CA, USA*

¹²*Auckland Observatory, Box 24180, Auckland, New Zealand*

¹³*European Southern Observatory, Karl-Schwarzschild-Str. 2, 85748 Garching, Germany*

¹⁴*Department of Physics and Astronomy, Vanderbilt University, Nashville, TN 37235, USA*

¹⁵*Kumeu Observatory, Kumeu, New Zealand*

¹⁶*Shandong Provincial Key Laboratory of Optical Astronomy and Solar-Terrestrial Environment, Institute of Space Sciences, Shandong University, Weihai 264209, People's Republic of China*

¹⁷*Department of Astronomy Ohio State University, 140 W. 18th Ave., Columbus, OH 43210, USA*

¹⁸*Center for Cosmology and AstroParticle Physics (CCAPP), The Ohio State University, 191 W. Woodruff Avenue, Columbus, OH 43210, USA.*

¹⁹*Antelope Hills Observatory, 980 Antelope Drive West, Bennett, CO 80102, USA*

²⁰*Institute of Astronomy and National Astronomical Observatory, Bulgarian Academy of Sciences, 72 Tsarigradsko Shose Blvd., 1784 Sofia, Bulgaria*

²¹*Department of Astronomy, Faculty of Physics, University of Sofia, 1164 Sofia, Bulgaria*

²²*Department of Physics and Astronomy, University of Iowa*

²³*Institute for Radio Astronomy and Space Research, AUT University, Auckland, New Zealand*

²⁴*Department of Particle Physics and Astrophysics, Weizmann Institute of Science, Rehovot 76100, Israel*

²⁵*Steward Observatory, University of Arizona, 933 North Cherry Avenue, Tucson, AZ 85721, USA*

²⁶*Center for Backyard Astrophysics Belgium, Walhostraat 1A, B-3401 Landen, Belgium*

²⁷*Canadian Institute for Theoretical Astrophysics, University of Toronto, 60 St George Street, Toronto, ON M5S 3H8, Canada*

ABSTRACT

We report the lens mass and distance measurements of the nearby microlensing event TCP J05074264+2447555. We measure the microlens parallax vector π_E using *Spitzer* and ground-based light curves with constraints on the direction of lens-source relative proper motion derived from Very Large Telescope Interferometer (VLTI) GRAVITY observations. Combining this π_E determination with the angular Einstein radius θ_E measured by VLTI GRAVITY observations, we find that the lens is a star with mass $M = 0.495 \pm 0.063 M_\odot$ at a distance $D_L = 429 \pm 21$ pc. We find that the blended light basically all comes from the lens. The lens-source proper motion is $\mu_{\text{rel, hel}} = 26.55 \pm 0.36$ mas yr⁻¹, so with currently available adaptive-optics (AO) instruments, the lens and source can be resolved in 2021. This is the first microlensing event whose lens mass is unambiguously measured by interferometry + satellite parallax observations, which opens a new window for mass measurements of isolated objects such as stellar-mass black holes.

1. INTRODUCTION

Gravitational microlensing offers a unique window into probing extrasolar planets beyond the snow line (Mao & Paczynski 1991; Gould & Loeb 1992; Mao 2012; Gaudi 2012) and isolated dark objects such as free-floating planets (Sumi et al. 2011; Mróz et al. 2017, 2018, 2019), brown dwarfs (Gould et al. 2009; Shvartzvald et al. 2019) and black holes (Gould 2000b; Mao et al. 2002; Bennett et al. 2002; Wyrzykowski et al. 2016). For a typical microlensing event, the only measured observable that relates to the physical properties of the lens is the Einstein timescale t_E . It is a combination of the lens mass M_L , the lens-source relative proper motion μ_{rel} and parallax π_{rel} by

$$t_E = \frac{\theta_E}{\mu_{\text{rel}}}; \quad \theta_E = \sqrt{\kappa M_L \pi_{\text{rel}}}; \quad \pi_{\text{rel}} = \pi_L - \pi_S, \quad (1)$$

where $\kappa \equiv 4G/(c^2 \text{AU}) = 8.144 \text{ mas}/M_\odot$, θ_E is the angular Einstein radius, $\pi_L = \text{AU}/D_L$ and $\pi_S = \text{AU}/D_S$ are the lens and source parallax, respectively, and D_L and D_S are the lens and the source distances, respectively. Therefore, with only t_E known, the lens mass and distance cannot be unambiguously determined. By far, the most common way to break this degeneracy is to also measure the angular Einstein radius θ_E and the microlens parallax π_E . For a lensing object, its mass is related to these two observables by (Gould 1992, 2000a)

$$M_L = \frac{\theta_E}{\kappa \pi_E}, \quad (2)$$

and the lens-source relative proper motion and parallax by

$$\mu_{\text{rel}} = \frac{\theta_E}{t_E} \frac{\pi_E}{\pi_E}; \quad \pi_{\text{rel}} = \theta_E \pi_E, \quad (3)$$

where the microlens parallax vector π_E is defined by

$$\pi_E \equiv \frac{\pi_{\text{rel}} \mu_{\text{rel}}}{\theta_E \mu_{\text{rel}}}. \quad (4)$$

There are three methods to measure the microlens parallax π_E . The first one is “orbital microlens parallax”, which is due to the Earth’s orbital acceleration around the Sun that introduces deviation from rectilinear motion in the lens-source relative motion (Gould 1992). However, this method is generally only feasible for events with long microlensing timescales $t_E \gtrsim \text{year}/2\pi$ (e.g., Udalski et al. 2018) and/or events produced by nearby lenses (e.g., Jung et al. 2018). The second method is “terrestrial microlens parallax” (Hardy & Walker 1995; Holz & Wald 1996), which in rare cases can be measured by a combination of simultaneous observations from well-separated ground-based telescopes (e.g., Gould et al. 2009; Yee et al. 2009). The most efficient and robust way to measure π_E is via “satellite microlens parallax”, which is done by observing the same microlensing event from Earth and one or more well-separated ($\sim \text{AU}$) satellite (Refsdal 1966; Gould 1994, 1995). The first observed example applying this method was the event OGLE-2005-SMC-001 (Dong et al. 2007), in which the joint analysis of ground-based observations and *Spitzer* observations indicates that the lens is probably a halo binary. Microlens parallax measurements from two satellites (*Spitzer* and the two-wheel *Kepler* K2) have also been achieved to measure the parallax of the event OGLE-2016-BLG-0975 (Zhu et al. 2017a). Since 2014, the *Spitzer* satellite has observed about 1000 microlensing events toward the Galactic bulge (Gould et al. 2013, 2014, 2015b,a, 2016, 2018), in order to probe planets in substantially different Galactic environments (Calchi Novati et al. 2015a; Zhu et al. 2017b), and they have yielded unambiguous mass measurements for seven planetary systems (Udalski et al. 2015; Street et al. 2016; Ryu et al. 2018; Shvartzvald et al. 2017; Calchi Novati et al. 2018; Jung et al. 2019; Gould et al. 2019).

The angular Einstein radius θ_E is generally measured via finite-source effects (Gould 1994; Witt & Mao 1994; Nemiroff & Wickramasinghe 1994) when the source transits a caustic (where the magnification diverges to infinity) or comes close to a cusp. The detection of finite-source effects usually yields the source radius normalized by the Einstein radius, ρ , and combining it with the source angular radius θ_* , which is routinely determined from the intrinsic color and de-reddened brightness of the source (Yoo et al. 2004), can lead to the measurement of the angular Einstein radius $\theta_E = \theta_*/\rho$. Finite-source effects are frequently detected in binary/planetary events due to their relatively large caustic structures, but they are rarely measured in a single-lens event since its caustic is a single geometric point.

Besides the mass measurements from combining the angular Einstein radius θ_E and the microlens parallax π_E , an independent mass-distance relationship can be obtained if the flux from the lens system is measured with high angular resolution imaging and compared to stellar models (see, e.g., Bennett et al. 2007; Yee 2015). These are achieved either by measuring the flux at the position of the source star in excess of the source flux to constrain the lens flux (e.g., Koshimoto et al. 2017a,b), or in some cases,

resolving the source and lens $\sim 5\text{--}20$ years after the microlensing event and thus directly measure the lens flux (e.g., [Alcock et al. 2001](#); [Batista et al. 2015](#); [Bennett et al. 2015](#); [Bhattacharya et al. 2018](#)). The additional mass-distance relationship from the lens flux, combined with the constraints from the angular Einstein radius θ_E and/or the microlens parallax, can yield the mass and distance of the lens system (e.g., [Dong et al. 2009](#); [Beaulieu et al. 2018](#)). However, this method is not feasible for dark lenses such as free-floating planets and black holes.

Here we report the lens mass measurement of the nearby microlensing event TCP J05074264+2447555 (hereafter referred to as “TCP J0507+2447” for brevity) by a joint analysis of ground-based, *Spitzer*, and VLTI GRAVITY observations of [Dong et al. \(2019\)](#). The paper is structured as follows. In § 2, we introduce the ground-based and *Spitzer* observations. We then describe the light curve modeling process in § 3. In § 4, we derive the physical parameters of the lens. Finally, we discuss the implications of our work in § 5.

2. OBSERVATIONS

TCP J0507+2447, at equatorial coordinates $(\alpha, \delta)_{J2000} = (05:07:42.72, +24:47:56.4)$, [Gaia Collaboration et al. 2018](#)), corresponding to Galactic coordinates $(\ell, b) = (178.76, -9.33)$, was first discovered by the Japanese amateur astronomer Tadashi Kojima (Gunma-ken, Japan) on UT 2017-10-25.688. For ground-based data, we choose the light curves used by [Dong et al. \(2019\)](#), including the data from All-Sky Automatic Survey for Supernovae (ASAS-SN; [Shappee et al. 2014](#)), 0.6 m telescopes at Post Observatory (RP), 0.5 m Iowa Robotic Telescope (Iowa) at the Winer Observatory (Arizona, USA), 0.4m telescope at Auckland Observatory (AO), and the 1.3m SMARTS telescope ([DePoy et al. 2003](#)) at Cerro Tololo Inter-American Observatory (CTIO). We supplement it with CTIO *V*-band data to derive the *VHL* color-color relation. All the ground-based data were calibrated to standard magnitude systems. For further descriptions of our ground-based data and their availability in digital format, see Appendix § B.

For *Spitzer*, we submitted a Director Discretion Time (DDT) proposal ([Dong et al. 2017](#)) to observe the TCP J0507+2447 on 2017 November 7, and it was approved on 2017 November 9. Due to the Sun-angle limit, it did not start taking observations until 2017 December 19 ($HJD' = 8107.2$, $HJD' = HJD - 2450000$). The observations ended on 2018 January 23 ($HJD' = 8143.7$). In total, 21 data points were taken, all using the $3.6\ \mu\text{m}$ channel (*L*-band) of the IRAC camera. The data were reduced by the method presented by [Calchi Novati et al. \(2015b\)](#).

3. LIGHT CURVE ANALYSIS

Figure 1 shows the TCP J0507+2447 data together with the best-fit single-lens model. In this section, we analyze the data with a single-lens model. [Nucita et al. \(2018\)](#) reported a short-duration planetary anomaly near the peak of the event, and we discuss the planetary-lens modeling in Appendix § A, in order to double check whether the measurements of the microlens parallax π_E is affected by the planetary model.

3.1. Ground-based data only

The single-lens model has three parameters t_0, u_0, t_E ([Paczynski 1986](#)) to calculate the magnification as a function of time $A(t)$: the time of the maximum magnification t_0 , the impact parameter u_0 (in units of the angular Einstein radius θ_E), and the Einstein radius crossing time t_E . For each data set i , we introduce two flux parameters ($f_{S,i}, f_{B,i}$) in order to model the observed flux $f_i(t)$ as

$$f_i(t) = f_{S,i}A(t) + f_{B,i}, \quad (5)$$

where $f_{S,i}$ represents the flux of the source star, and $f_{B,i}$ represents any blended flux that is not lensed in the photometric aperture. In addition, to fit the orbital microlens parallax, we parameterize the microlens parallax effects by $\pi_{E,N}$ and $\pi_{E,E}$, which are the North and East components of the microlens parallax vector ([Gould 2004](#)), respectively. We also fit $u_{0,\oplus} > 0$ and $u_{0,\oplus} < 0$ solutions to consider the “ecliptic degeneracy” ([Jiang et al. 2004](#); [Poindexter et al. 2005](#)). We find $\pi_E = 0.13 \pm 0.47$ for the $u_{0,\oplus} > 0$ solution and $\pi_E = 0.67 \pm 0.52$ for the $u_{0,\oplus} < 0$ solution. The likelihood distributions of $(\pi_{E,N}, \pi_{E,E})$ from ground-based data are shown in Figure 2.

3.2. Satellite parallax

For TCP J0507+2447, *Spitzer* took observations in $1.7 < (t - t_{0,\oplus})/t_E < 3.1$. We can estimate the microlens parallax by

$$\tilde{\pi}_E \sim \frac{au}{D_\perp} (\Delta\tau, \Delta\beta), \quad \Delta\tau \equiv \frac{t_{0,Spitzer} - t_{0,\oplus}}{t_E}, \quad \Delta\beta \equiv \pm u_{0,Spitzer} - \pm u_{0,\oplus}, \quad (6)$$

where D_{\perp} is the projected separation between the *Spitzer* satellite¹ and Earth at the time of the event. Generally, the four possible values of $\Delta\beta$ result in a set of four degenerate solutions (Refsdal 1966; see also Figure 1 from Gould 1994). However, the four solutions merge into two disjoint ($u_{0,\oplus} > 0$ and $u_{0,\oplus} < 0$) solutions because the *Spitzer* data commence well after $t_{0,Spitzer}$ (Gould 2019). In addition, we include a *VHL* color-color constraint on the *Spitzer* source flux $f_{s,Spitzer}$ (e.g., Calchi Novati et al. 2015a), which adds a χ_{Color}^2 into the total χ_{total}^2 ,

$$\chi_{\text{Color}}^2 = \frac{[(V - L)_S - (V - L)_{\text{fix}}]^2}{\sigma_{\text{cc}}^2}, \quad (7)$$

where $(V - L)_S$ is the source color from the modeling, $(V - L)_{\text{fix}}$ is the color constraint, and σ_{cc} is the uncertainty of the color constraint. To derive the color constraint, we extract the CTIO *V*- and *H*- band and *Spitzer L*-band photometry for stars within 1' (10 stars in total), and fit for the two parameters c_0 and c_1 in the equation

$$V_{\text{CTIO}} - L_{\text{Spitzer}} = c_0 + c_1(V_{\text{CTIO}} - H_{\text{CTIO}} - X_p), \quad (8)$$

where $X_p = 3.14$ is a pivot parameter chosen to minimize the covariance between c_0 and c_1 . We get $c_0 = 2.370 \pm 0.016$, $c_1 = 0.988 \pm 0.043$. We derive the source color by regression of CTIO *V* versus *H* flux as the source magnification changes, and find $(V_{\text{CTIO}} - H_{\text{CTIO}})_S = 2.096 \pm 0.024$, $(V - L)_{\text{fix}} = 1.34 \pm 0.06$. We apply the color constraint to the modeling and find $\pi_E = 0.68 \pm 0.23$ for the $u_{0,\oplus} > 0$ solution and $\pi_E = 1.01 \pm 0.34$ for the $u_{0,\oplus} < 0$ solution.

The measured satellite parallax above is a combination of orbital parallax and satellite parallax. To investigate the satellite parallax from the *Spitzer* data, we fix $(t_0, u_{0,\oplus}, t_E)$ from the best-fit non-parallax model, and fit the parallax only with *Spitzer* data and the color constraint. We find the resulting “Ground + *Spitzer*” parallax is an intersection of the satellite parallax, which is nearly a circle, and the orbital parallax, which is nearly a straight line. Gould (2019) shows that the nearly circular shape of the satellite-parallax contours are due to partial overlap of a series of osculating, exactly circular, degeneracies in the π_E plane, and similar satellite-parallax shapes have been detected in two *Spitzer* planetary events (Jung et al. 2019; Gould et al. 2019). The best-fit parameters for the $u_{0,\oplus} > 0$ and $u_{0,\oplus} < 0$ solutions are shown in Tables 2 and 3, respectively. The likelihood distributions of $(\pi_{E,N}, \pi_{E,E})$ from “*Spitzer*-only” and “Ground + *Spitzer*” are shown in Figure 2.

3.3. VLTI constraint on the parallax direction

VLTI GRAVITY provides constraints on the direction of the lens-source relative proper motion and thus (see Equation 4) the direction of the microlens parallax (see Figure 4 of Dong et al. 2019). For the “no lens light” model, the direction of the microlens parallax (North through East)

$$\Phi_{\text{VLTI}} = \begin{cases} 192.9^\circ \pm 0.4^\circ & \text{for } u_{0,\oplus} < 0 \\ 156.1^\circ \pm 0.4^\circ & \text{for } u_{0,\oplus} > 0, \end{cases} \quad (9)$$

and for the “luminous lens” model,

$$\Phi_{\text{VLTI}} = \begin{cases} 193.5^\circ \pm 0.4^\circ & \text{for } u_{0,\oplus} < 0 \\ 156.7^\circ \pm 0.4^\circ & \text{for } u_{0,\oplus} > 0. \end{cases} \quad (11)$$

We include the constraint of the parallax direction by adding a χ_{VLTI}^2 into the total χ_{total}^2 ,

$$\chi_{\text{VLTI}}^2 = \frac{(\Phi_{\text{model}} - \Phi_{\text{VLTI}})^2}{\sigma_{\text{VLTI}}^2}, \quad (13)$$

where Φ_{VLTI} is the parallax direction from the modeling, and $\sigma_{\text{VLTI}} = 0.4^\circ$ is the uncertainty of the VLTI parallax direction. The best-fit parameters are shown in Tables 2 and 3, and its likelihood distributions of $(\pi_{E,N}, \pi_{E,E})$ are shown in Figure 3. For both the “no lens light” model and the “luminous lens” model, the $u_{0,\oplus} < 0$ solution is disfavored by $\Delta\chi^2 > 41$. Actually, from the likelihood distributions of $(\pi_{E,N}, \pi_{E,E})$ from “Ground + *Spitzer*” data shown in Figure 2, we can see that the VLTI parallax direction for the $u_{0,\oplus} < 0$ solution is inconsistent with the constraint from the “Ground + *Spitzer*” data. Thus, we reject the $u_{0,\oplus} < 0$ solution.

¹ We extract the geocentric locations of *Spitzer* from the *JPL Horizons* website: <http://ssd.jpl.nasa.gov/?horizons>

4. PHYSICAL PARAMETERS

4.1. Is the lens luminous?

For the “no lens light” model, VLTI measured the angular Einstein radius $\theta_E = 1.850 \pm 0.014$ mas, and the light curve modeling shows $\pi_E = 0.476 \pm 0.061$, so the lens mass $M_L = 0.477 \pm 0.061 M_\odot$ and the lens source relative parallax $\pi_{\text{rel}} = \theta_E \pi_E = 0.880 \pm 0.113$ mas. The parallax of the “baseline object” has been measured by *Gaia* second data release (DR2) (Gaia Collaboration et al. 2018; Bailer-Jones et al. 2018)

$$\pi_{\text{base}} = 1.480 \pm 0.031 \text{ mas} \quad (14)$$

which is the flux-weighted mean parallax of the source and the blend in *Gaia* band,

$$\pi_{\text{base}} = \eta \pi_B + (1 - \eta) \pi_S, \quad (15)$$

where η is the fraction of total *Gaia* flux due to the blending, π_B is the parallax of the blending. The *Gaia* band is qualitatively similar to *V* band, and the best-fit solution of the “no lens light” model has $f_{B,V}/f_{S,V} \sim 0.04$, so we estimate $\pi_S \sim \pi_{\text{base}}$, and $D_L = \text{AU}/(\pi_{\text{rel}} + \pi_S) = 424 \pm 14$ pc. Using the MIST isochrones² with age ≥ 2 Gyr, the lens has an absolute *K*-band magnitude of $K_{L,0} = 5.7 \pm 0.3$. Dong et al. (2019) has found that the source suffers from an extinction $A_{K,S} = 0.155$, we thus estimate the extinction of the lens $A_{K,L} \sim A_{K,S} D_L/D_S = 0.097$. As a result, the apparent *K*-band magnitude of the lens is

$$K_L = K_{L,0} + 5 \log \frac{D_L}{10 \text{ pc}} + A_{K,L} = 13.9 \pm 0.3, \quad (16)$$

which is $\sim 13\%$ of the 2MASS baseline $K = 11.680 \pm 0.018$. Thus, the lens is luminous, and we reject the “no lens light” model.

4.2. Blend = Lens?

Table 4 shows the blend in *H*-, *I*-, *R*-, *V*- bands from the best-fit “luminous lens” model, which shows that the blend is detected in all bands. To estimate the lens apparent brightness, we use the angular Einstein radius $\theta_E = 1.891 \pm 0.014$ mas and $\pi_E = 0.469 \pm 0.060$ of the “luminous lens” model, and follow the procedure in Section 4.1. For extinction, we adopt the extinction law of Cardelli et al. (1989) and estimate the extinction of the lens in λ band $A_{\lambda,L} \sim A_{\lambda,S} D_L/D_S$. The predicted lens apparent magnitude is shown in Table 4. We find that the predicted lens apparent magnitude is consistent with the blend within 1σ in all bands. Thus, the blended light basically all comes from the lens.

4.3. Lens parameters

According to the best-fit “luminous lens” model, the lens mass

$$M = \frac{\theta_E}{\kappa \pi_E} = 0.495 \pm 0.063 M_\odot, \quad (17)$$

the lens-source relative parallax

$$\pi_{\text{rel}} = \theta_E \pi_E = 0.887 \pm 0.114 \text{ mas}. \quad (18)$$

Combining Equations (1), (14) and (15), we obtain

$$\pi_L = \pi_{\text{base}} + (1 - \eta) \pi_{\text{rel}} = 2.332 \pm 0.114 \text{ mas}; \quad D_L = \frac{\text{AU}}{\pi_L} = 429 \pm 21 \text{ pc}, \quad (19)$$

where we adopt $\eta = f_{B,V}/(f_{S,V} + f_{B,V}) = 0.040 \pm 0.016$ from the best-fit “luminous lens” model as the fraction of total *Gaia* flux due to the lens. The geocentric and heliocentric relative proper motion are

$$\boldsymbol{\mu}_{\text{rel,geo}}(N, E) = \frac{\theta_E}{t_E} \frac{\boldsymbol{\pi}_E}{\pi_E} = (-22.73, 9.83) \pm (0.21, 0.19) \text{ mas yr}^{-1}; \quad (20)$$

$$\boldsymbol{\mu}_{\text{rel,hel}}(N, E) = \boldsymbol{\mu}_{\text{rel,geo}} + \frac{\pi_{\text{rel}}}{\text{AU}} \mathbf{v}_{\oplus,\perp} = (-22.45, 14.18) \pm (0.21, 0.59) \text{ mas yr}^{-1}, \quad (21)$$

² <http://waps.cfa.harvard.edu/MIST/interpisos.html>

where $\mathbf{v}_{\oplus,\perp} = (1.47, 23.29) \text{ km s}^{-1}$ is Earth’s projected velocity on the event at t_0 . The proper motion of the “baseline object” has been measured by *Gaia*

$$\boldsymbol{\mu}_{\text{base}}(N, E) = (-7.330, -0.228) \pm (0.033, 0.061) \text{ mas yr}^{-1}, \quad (22)$$

which is also the flux-weighted mean proper motion. Thus, the lens and source proper motion are

$$\boldsymbol{\mu}_{\text{L}}(N, E) = \boldsymbol{\mu}_{\text{base}} + (1 - \eta)\boldsymbol{\mu}_{\text{rel, hel}} = (-28.89, 13.39) \pm (0.41, 0.61) \text{ mas yr}^{-1}; \quad (23)$$

$$\boldsymbol{\mu}_{\text{S}}(N, E) = \boldsymbol{\mu}_{\text{base}} - \eta\boldsymbol{\mu}_{\text{rel, hel}} = (-6.43, -0.80) \pm (0.36, 0.23) \text{ mas yr}^{-1}. \quad (24)$$

We summarize the derived lens parameters in Table 5.

5. DISCUSSION AND CONCLUSION

We have reported the analysis of the microlensing event TCP J0507+2447. The combination of the angular Einstein radius θ_{E} measured by VLTI GRAVITY observations, and the direction of microlens parallax π_{E} constrained from VLTI GRAVITY observations, *Spitzer* observations and ground-based observations, reveals that the lens is a $M_{\text{L}} = 0.495 \pm 0.063 M_{\odot}$ star at $D_{\text{L}} = 429 \pm 21 \text{ pc}$. We also note that Fukui et al. (2019) reported the lens mass and distance of TCP J0507+2447 to be $M_{\text{L}} = 0.581 \pm 0.033 M_{\odot}$ star at $D_{\text{L}} = 505 \pm 47 \text{ pc}$, which is a combination of finite-source effects, Keck AO image, spectroscopy, annual parallax and VLTI observations (see Table 4 and Figure 9 of Fukui et al. 2019). That is, their mass estimate is 1.2σ higher than ours. We note that Fukui et al. (2019) used spectroscopy to determine the source distance and got $D_{\text{S}} = 800 \pm 130 \text{ pc}$. If we adopt *Gaia* parallax, the angular Einstein radius θ_{E} measured by VLTI GRAVITY observations and the lens flux constraints of Fukui et al. (2019), we get $M_{\text{L}} = 0.527 \pm 0.032 M_{\odot}$ star at $D_{\text{L}} = 434 \pm 12 \text{ pc}$, which is in agreement with our measurements within 1σ . Using current AO instruments, Batista et al. (2015); Bennett et al. (2015); Bhattacharya et al. (2018) resolved the lens and source for cases that these have approximately equal brightness when they were separated by 34–60 mas. In this case, the lens-source proper motion is $\mu_{\text{rel, hel}} = 26.55 \pm 0.36 \text{ mas yr}^{-1}$, and the lens is about 1.8 mag fainter than the source in *H*-band. We estimate that it will probably require $\sim 80 \text{ mas}$ to resolve the source and lens. Thus, the derived physical parameters of our work can be verified by currently available AO instruments in 2021 and later.

This is the first microlensing event whose lens mass has been unambiguously measured by interferometry (VLTI GRAVITY) + satellite (*Spitzer*) parallax observations. Interferometry + satellite parallax is a new method to measure the mass of isolated objects. The detection frequency of finite-source effects in a single event is only $\sim 2\%$ (Zhu et al. 2016; Zang et al. 2019), so interferometric observation such as VLTI GRAVITY is a complementary approach to measurements of the angular Einstein radius θ_{E} . In addition, interferometry can provide additional constraints on the microlens parallax direction, which is helpful for breaking degeneracy in the parallax measurements (Refsdal 1966; Gould 1994). Gould (2000b) estimated that $\sim 20\%$ of Galactic microlensing events are caused by stellar remnants, and specifically that $\sim 1\%$ are due to stellar-mass black-hole lenses. Some black-hole candidates (Mao et al. 2002; Bennett et al. 2002; Wyrzykowski et al. 2016) have been reported by microlensing surveys, but none of these candidates had finite-source effects. Therefore, interferometry observations such as VLTI GRAVITY + satellite parallax opens up a new window for decisively confirming black-hole candidates by measuring their masses.

Nucita et al. (2018) reported a planetary companion in the TCP J0507+2447 lens system. Using the derived lens parameters, we infer the planet mass to be

$$M_{\text{planet}} = 19.0 \pm 3.0 M_{\oplus}. \quad (25)$$

The projected planet-host separation is

$$a_{\perp} = s\theta_{\text{E}}D_{\text{L}} \begin{cases} 0.76 \pm 0.04 \text{ AU for } s \sim 0.935; \\ 0.79 \pm 0.04 \text{ AU for } s \sim 0.975, \end{cases} \quad (26)$$

where s is the planet-host projected separation in units of θ_{E} . Following the procedure of Han et al. (2019), we estimate the radial-velocity (RV) amplitude $v \sin(i) \sim 2.3 \text{ m s}^{-1}$ with a period of $\sim 1.3 \text{ yr}$, which may be detectable by high-resolution spectrometers such as VLT/Espresso with 4 VLT telescopes. In addition, the snow line radius of the lens system is $a_{\text{SL}} \sim 2.7(M/M_{\odot}) = 1.3 \text{ AU}$ (Kennedy & Kenyon 2008). Thus, this is the first Neptune within the snow line detected by microlensing.

We thank Tianshu Wang and Jennifer Yee for fruitful discussions. We are grateful to Robin Leadbeater and Paolo Berardi for making their spectroscopic observations available to us during the observing campaign. S.D. and P.C. acknowledges Projects 11573003 supported by the National Science Foundation of China (NSFC). W.Z., H.Y., S.-S.L. and S.M. acknowledges support

by the National Science Foundation of China (Grant No. 11821303 and 11761131004). Work by AG was supported by AST-1516842 and by JPL grant 1500811. AG received support from the European Research Council under the European Unions Seventh Framework Programme (FP 7) ERC Grant Agreement n. [321035]. This work is based (in part) on observations made with the Spitzer Space Telescope, which is operated by the Jet Propulsion Laboratory, California Institute of Technology under a contract with NASA. Support for this work was provided by NASA through an award issued by JPL/Caltech. Work by S. M. Hu was supported by the Natural Science Foundation of Shandong province (No. JQ201702), and the Young Scholars Program of Shandong University (No. 20820162003). WZ was supported by the Beatrice and Vincent Tremaine Fellowship at CITA.

APPENDIX

A. THE PLANETARY MODEL

Nucita et al. (2018) reported a short-duration anomaly near the peak of the event, indicating that the lens star has a planetary companion with planet-host mass ratio $q = 1.1 \times 10^{-4}$. To double check the parallax measurements, we fit the event with the binary-lens model. Besides the three parameters t_0, u_0, t_E introduced in § 3.1, the binary-lens model has four other parameters (s, q, α, ρ). Here, q is the companion-host mass ratio, s is the companion-host projected separation in units of θ_E , α is the angle between the source trajectory and the binary axis in the lens plane, and ρ is the source radius normalized to θ_E .

We fix (s, q, α) as the best-fit values shown in Nucita et al. (2018). We include the satellite parallax and the constraints from VLTI GRAVITY. We consider the so-called “minor-image perturbation degeneracy” (e.g., Koshimoto et al. 2017b; Calchi Novati et al. 2019; Han et al. 2018) found by Nucita et al. (2018): $s = 0.935 \pm 0.004$ and $s = 0.975 \pm 0.004$. Table 6 shows the best-fit parameters. For all the solutions, the resulting parallax is consistent with the results of the single-lens model within 1σ . Thus, different models (single-lens and binary-lens) do not have significant influence on the parallax and thus the mass measurements.

B. GROUND-BASED PHOTOMETRIC OBSERVATIONS

We summarize the ground-based photometric observations collected during our observing campaign in Table B. The ASCII data will be made available upon publication.

Table 1. Ground-based Photometric Observations

Site	Filter
All-Sky Automatic Survey for Supernovae (ASAS-SN)	V
Cerro Tololo Inter-American Observatory (CTIO)	V, H
Post Observatory (RP)	B, V
Auckland Observatory (AO)	R, I
Iowa Robotic Telescope (Iowa)	r, i
Desert Bloom Observatory (DBO)	B, V, I, Clear
Coral Towers Observatory (CTO)	Clear
Kumeu Observatory (KO)	Wratten12
Weihai (WH) Observatory of Shandong University	B, V
Antelope Hill Observatory (ATO)	B, V
Bulgarian National Astronomical Observatory (Rozhen)	B, V
Peking University 40cm Telescope of (PFT)	UHC
Center for Backyard Astronomy Belgium Observatory (CBABO)	V, Clear

REFERENCES

- | | |
|--|--|
| Alcock, C., Allsman, R. A., Alves, D. R., et al. 2001, <i>Nature</i> , 414, 617 | Batista, V., Beaulieu, J.-P., Bennett, D. P., et al. 2015, <i>ApJ</i> , 808, 170 |
| Bailer-Jones, C. A. L., Rybizki, J., Fouesneau, M., Mantelet, G., & Andrae, R. 2018, <i>AJ</i> , 156, 58 | Beaulieu, J.-P., Batista, V., Bennett, D. P., et al. 2018, <i>AJ</i> , 155, 78 |
| | Bennett, D. P., Anderson, J., & Gaudi, B. S. 2007, <i>ApJ</i> , 660, 781 |

- Bennett, D. P., Becker, A. C., Calitz, J. J., et al. 2002, arXiv Astrophysics e-prints, astro-ph/0207006
- Bennett, D. P., Bhattacharya, A., Anderson, J., et al. 2015, *ApJ*, 808, 169
- Bhattacharya, A., Beaulieu, J. P., Bennett, D. P., et al. 2018, *AJ*, 156, 289
- Calchi Novati, S., Gould, A., Udalski, A., et al. 2015a, *ApJ*, 804, 20
- Calchi Novati, S., Gould, A., Yee, J. C., et al. 2015b, *ApJ*, 814, 92
- Calchi Novati, S., Skowron, J., Jung, Y. K., et al. 2018, *AJ*, 155, 261
- Calchi Novati, S., Suzuki, D., Udalski, A., et al. 2019, *AJ*, 157, 121
- Cardelli, J. A., Clayton, G. C., & Mathis, J. S. 1989, *ApJ*, 345, 245
- DePoy, D. L., Atwood, B., Belville, S. R., et al. 2003, in *Proc. SPIE*, Vol. 4841, Instrument Design and Performance for Optical/Infrared Ground-based Telescopes, ed. M. Iye & A. F. M. Moorwood, 827–838
- Dong, S., Carey, S., Gould, A., & Zhu, W. 2017, First Mass Measurement of a 'Domestic' Microlens, Spitzer Proposal, ,
- Dong, S., Udalski, A., Gould, A., et al. 2007, *ApJ*, 664, 862
- Dong, S., Gould, A., Udalski, A., et al. 2009, *ApJ*, 695, 970
- Dong, S., Mérand, A., Delplancke-Ströbele, F., et al. 2019, *ApJ*, 871, 70
- Fukui, A., Suzuki, D., Koshimoto, N., et al. 2019, arXiv e-prints, arXiv:1909.11802
- Gaia Collaboration, Brown, A. G. A., Vallenari, A., et al. 2018, *A&A*, 616, A1
- Gaudi, B. S. 2012, *ARA&A*, 50, 411
- Gould, A. 1992, *ApJ*, 392, 442
- . 1994, *ApJL*, 421, L75
- . 1995, *ApJL*, 441, L21
- . 2000a, *ApJ*, 542, 785
- . 2000b, *ApJ*, 535, 928
- . 2004, *ApJ*, 606, 319
- . 2019, *JKAS*, 52, 121
- Gould, A., Carey, S., & Yee, J. 2013, Spitzer Microlens Planets and Parallaxes, Spitzer Proposal, ,
- . 2014, Galactic Distribution of Planets from Spitzer Microlens Parallaxes, Spitzer Proposal, ,
- . 2016, Galactic Distribution of Planets Spitzer Microlens Parallaxes, Spitzer Proposal, ,
- Gould, A., & Loeb, A. 1992, *ApJ*, 396, 104
- Gould, A., Yee, J., & Carey, S. 2015a, Degeneracy Breaking for K2 Microlens Parallaxes, Spitzer Proposal, ,
- . 2015b, Galactic Distribution of Planets From High-Magnification Microlensing Events, Spitzer Proposal, ,
- Gould, A., Yee, J., Carey, S., & Shvartzvald, Y. 2018, The Galactic Distribution of Planets via Spitzer Microlensing Parallax, Spitzer Proposal, ,
- Gould, A., Udalski, A., Monard, B., et al. 2009, *ApJL*, 698, L147
- Gould, A., Ryu, Y.-H., Calchi Novati, S., et al. 2019, arXiv e-prints, arXiv:1906.11183
- Han, C., Bond, I. A., Gould, A., et al. 2018, *AJ*, 156, 226
- Han, C., Yee, J. C., Udalski, A., et al. 2019, *AJ*, 158, 102
- Hardy, S. J., & Walker, M. A. 1995, *MNRAS*, 276, L79
- Holz, D. E., & Wald, R. M. 1996, *ApJ*, 471, 64
- Jiang, G., DePoy, D. L., Gal-Yam, A., et al. 2004, *ApJ*, 617, 1307
- Jung, Y. K., Han, C., Udalski, A., et al. 2018, *ApJ*, 863, 22
- Jung, Y. K., Gould, A., Udalski, A., et al. 2019, *AJ*, 158, 28
- Kennedy, G. M., & Kenyon, S. J. 2008, *ApJ*, 673, 502
- Koshimoto, N., Shvartzvald, Y., Bennett, D. P., et al. 2017a, *AJ*, 154, 3
- Koshimoto, N., Udalski, A., Beaulieu, J. P., et al. 2017b, *AJ*, 153, 1
- Mao, S. 2012, *Research in Astronomy and Astrophysics*, 12, 947
- Mao, S., & Paczynski, B. 1991, *ApJL*, 374, L37
- Mao, S., Smith, M. C., Woźniak, P., et al. 2002, *MNRAS*, 329, 349
- Mróz, P., Udalski, A., Skowron, J., et al. 2017, *Nature*, 548, 183
- Mróz, P., Ryu, Y.-H., Skowron, J., et al. 2018, *AJ*, 155, 121
- Mróz, P., Udalski, A., Bennett, D. P., et al. 2019, *A&A*, 622, A201
- Nemiroff, R. J., & Wickramasinghe, W. A. D. T. 1994, *ApJL*, 424, L21
- Nucita, A. A., Licchelli, D., De Paolis, F., et al. 2018, *MNRAS*, 476, 2962
- Paczynski, B. 1986, *ApJ*, 304, 1
- Poindexter, S., Afonso, C., Bennett, D. P., et al. 2005, *ApJ*, 633, 914
- Refsdal, S. 1966, *MNRAS*, 134, 315
- Ryu, Y.-H., Yee, J. C., Udalski, A., et al. 2018, *AJ*, 155, 40
- Shappee, B. J., Prieto, J. L., Grupe, D., et al. 2014, *ApJ*, 788, 48
- Shvartzvald, Y., Yee, J. C., Calchi Novati, S., et al. 2017, *ApJL*, 840, L3
- Shvartzvald, Y., Yee, J. C., Skowron, J., et al. 2019, *AJ*, 157, 106
- Street, R. A., Udalski, A., Calchi Novati, S., et al. 2016, *ApJ*, 819, 93
- Sumi, T., Kamiya, K., Bennett, D. P., et al. 2011, *Nature*, 473, 349
- Udalski, A., Yee, J. C., Gould, A., et al. 2015, *ApJ*, 799, 237
- Udalski, A., Ryu, Y.-H., Sajadian, S., et al. 2018, *AcA*, 68, 1
- Witt, H. J., & Mao, S. 1994, *ApJ*, 430, 505
- Wyrzykowski, Ł., Kostrzewa-Rutkowska, Z., Skowron, J., et al. 2016, *MNRAS*, 458, 3012
- Yee, J. C. 2015, *ApJL*, 814, L11
- Yee, J. C., Udalski, A., Sumi, T., et al. 2009, *ApJ*, 703, 2082
- Yoo, J., DePoy, D. L., Gal-Yam, A., et al. 2004, *ApJ*, 603, 139
- Zang, W., Shvartzvald, Y., Wang, T., et al. 2019, arXiv e-prints, arXiv:1904.11204
- Zhu, W., Calchi Novati, S., Gould, A., et al. 2016, *ApJ*, 825, 60
- Zhu, W., Udalski, A., Huang, C. X., et al. 2017a, *ApJL*, 849, L31
- Zhu, W., Udalski, A., Calchi Novati, S., et al. 2017b, *AJ*, 154, 210

Table 2. Best-fit parameters and their 68% uncertainty range from MCMC for the $u_{0,\oplus} > 0$ solutions

Parameters	$u_{0,\oplus} > 0$				
	non-parallax	w/o <i>Spitzer</i>	w/ <i>Spitzer</i>	VLTI + <i>Spitzer</i> (w/o lens light)	VLTI + <i>Spitzer</i> (w/ lens light)
$t_{0,\oplus}$ (HJD')	8058.76(1)	8058.76(1)	8058.76(1)	8058.76(1)	8058.76(1)
$u_{0,\oplus}$	0.083(1)	0.084(1)	0.084(1)	0.085(1)	0.084(1)
t_E	28.25(15)	27.98(42)	27.89(32)	27.83(15)	27.89(15)
$\pi_{E,N}$	-	0.11(83)	0.68(56)	-0.435(56)	-0.430(55)
$\pi_{E,E}$	-	0.06(13)	0.01(11)	0.193(24)	0.186(24)
π_E	-	0.13(47)	0.68(23)	0.476(61)	0.469(60)
$V_{CTIO,S}$	14.18(1)	14.17(2)	14.17(2)	14.15(1)	14.16(1)
$V_{CTIO,B}$	17.17(10)	17.38(32)	17.36(27)	17.58(16)	17.55(15)
$H_{CTIO,S}$	12.04(1)	12.03(2)	12.03(2)	12.02(1)	12.02(1)
$H_{CTIO,B}$	13.69(3)	13.74(8)	13.74(7)	13.79(3)	13.78(3)
χ^2_{Color}	-	-	0.040	0.002	0.047
χ^2_{VLTI}	-	-	-	0.014	0.003
χ^2_{total}/dof	557.82/558	556.9/556	576.2/575	576.7/575	576.6/575

Table 3. Best-fit parameters and their 68% uncertainty range from MCMC for the $u_{0,\oplus} < 0$ solutions

Parameters	$u_{0,\oplus} < 0$				
	non-parallax	w/o <i>Spitzer</i>	w/ <i>Spitzer</i>	VLTI + <i>Spitzer</i> (w/o lens light)	VLTI + <i>Spitzer</i> (w/ lens light)
$t_{0,\oplus}$ (HJD')	8058.76(1)	8058.76(1)	8058.76(1)	8058.76(1)	8058.76(1)
$u_{0,\oplus}$	-0.083	-0.084(1)	-0.084(1)	-0.084(1)	-0.082(1)
t_E	28.26(16)	28.11(45)	28.24(38)	28.06(35)	28.15(29)
$\pi_{E,N}$	-	0.67(81)	1.01(63)	-0.003(234)	-0.003(223)
$\pi_{E,E}$	-	-0.01(16)	-0.07(13)	-0.001(50)	-0.001(51)
π_E	-	0.67(52)	1.01(34)	0.003(239)	0.003(229)
$V_{CTIO,S}$	14.18(1)	14.16(2)	14.17(2)	14.17(1)	14.17(1)
$V_{CTIO,B}$	17.17(10)	17.40(34)	17.33(29)	17.27(27)	17.22(23)
$H_{CTIO,S}$	12.04(1)	12.02(2)	12.03(2)	12.03(1)	12.04(1)
$H_{CTIO,B}$	13.69(3)	13.75(8)	13.73(7)	13.71(6)	13.70(6)
χ^2_{Color}	-	-	0.002	39.840	40.728
χ^2_{VLTI}	-	-	-	0.033	0.009
χ^2_{total}/dof	557.83/558	556.7/556	576.2/575	618.2/575	618.0/575

Table 4. Blend from the best-fit “luminous lens” model versus the predicted apparent magnitude of the lens

Band	H	I	R	V
Extinction A_λ	0.10	0.42	0.66	0.87
Blending	13.78 ± 0.03	16.30 ± 0.07	16.76 ± 0.10	17.55 ± 0.15
Predicted lens apparent magnitude	13.9 ± 0.3	16.2 ± 0.4	16.7 ± 0.6	17.6 ± 0.8

Table 5. Physical parameters for the lens of TCP J0507+2447

$M_L [M_\odot]$	0.495 ± 0.063
$D_L [\text{pc}]$	429 ± 21
$D_S [\text{pc}]$	692 ± 15
$\mu_{L,\text{hel},N} [\text{mas yr}^{-1}]$	28.89 ± 0.41
$\mu_{L,\text{hel},S} [\text{mas yr}^{-1}]$	13.39 ± 0.61
$\mu_{S,\text{hel},N} [\text{mas yr}^{-1}]$	-6.42 ± 0.36
$\mu_{S,\text{hel},S} [\text{mas yr}^{-1}]$	-0.80 ± 0.23
$\mu_{\text{rel},\text{hel},N} [\text{mas yr}^{-1}]$	-22.45 ± 0.21
$\mu_{\text{rel},\text{hel},E} [\text{mas yr}^{-1}]$	14.18 ± 0.59
$\mu_{\text{rel},\text{geo},N} [\text{mas yr}^{-1}]$	-22.73 ± 0.21
$\mu_{\text{rel},\text{geo},E} [\text{mas yr}^{-1}]$	9.83 ± 0.19

Table 6. Binary-lens fitting results with the VLTI constraints

Parameters	$s = 0.935$				$s = 0.975$			
	$u_{0,\oplus} > 0$		$u_{0,\oplus} < 0$		$u_{0,\oplus} > 0$		$u_{0,\oplus} < 0$	
	w/o lens light	w/ lens light	w/o lens light	w/ lens light	w/o lens light	w/ lens light	w/o lens light	w/ lens light
$t_{0,\oplus} \text{ (HJD')}$	8058.76(1)	8058.76(1)	8058.76(1)	8058.76(1)	8058.76(1)	8058.76(1)	8058.78(1)	8058.76(1)
$u_{0,\oplus}$	0.086(1)	0.086(1)	-0.094(1)	-0.086(3)	0.086(1)	0.086(1)	-0.079	-0.084
t_E	27.82(16)	27.82(16)	28.10(41)	28.04(67)	27.81(17)	27.84(16)	29.61(48)	28.15(37)
$q(10^{-4})$	1.1	1.1	1.1	1.1	1.1	1.1	1.1	1.1
$\alpha \text{ (rad)}$	1.625	1.625	4.658	4.658	1.516	1.516	4.767	4.767
$\rho(10^{-3})$	5.5(6)	5.5(6)	81(16)	5.6(8)	5.8(6)	6.1(6)	5.1(5)	6.1(6)
$\pi_{E,N}$	-0.427(57)	-0.433(56)	-0.014(337)	-0.023(435)	-0.445(56)	-0.432(58)	-0.004(292)	-0.004(287)
$\pi_{E,E}$	0.189(25)	0.188(23)	-0.003(76)	-0.006(102)	0.197(24)	0.186(25)	-0.001(66)	-0.001(65)
π_E	0.467(62)	0.472(61)	0.015(346)	0.024(447)	0.486(61)	0.470(63)	0.004(299)	0.004(295)
$V_{\text{CTIO},S}$	14.15(1)	14.15(1)	14.17(2)	14.16(3)	14.15(1)	14.15(1)	14.17(3)	14.17(3)
$V_{\text{CTIO},B}$	17.71(20)	17.68(19)	17.38(41)	17.39(62)	17.70(20)	17.71(20)	17.29(52)	17.28(53)
$H_{\text{CTIO},S}$	12.02(1)	12.02(1)	12.03(2)	12.03(3)	12.02(1)	12.02(1)	12.03(3)	12.03(3)
$H_{\text{CTIO},B}$	13.81(4)	13.81(4)	13.74(10)	13.74(14)	13.81(4)	13.81(4)	13.72(13)	13.71(13)
χ^2_{Color}	0.026	0.019	41.722	41.891	0.027	0.058	41.643	41.274
χ^2_{VLTI}	0.040	0.114	0.074	0.028	0.024	0.026	0.202	0.390
$\chi^2_{\text{total}}/\text{dof}$	575.1/554	575.2/554	618.9/574	619.0/574	575.3/574	575.2/574	617.8/574	617.2/574

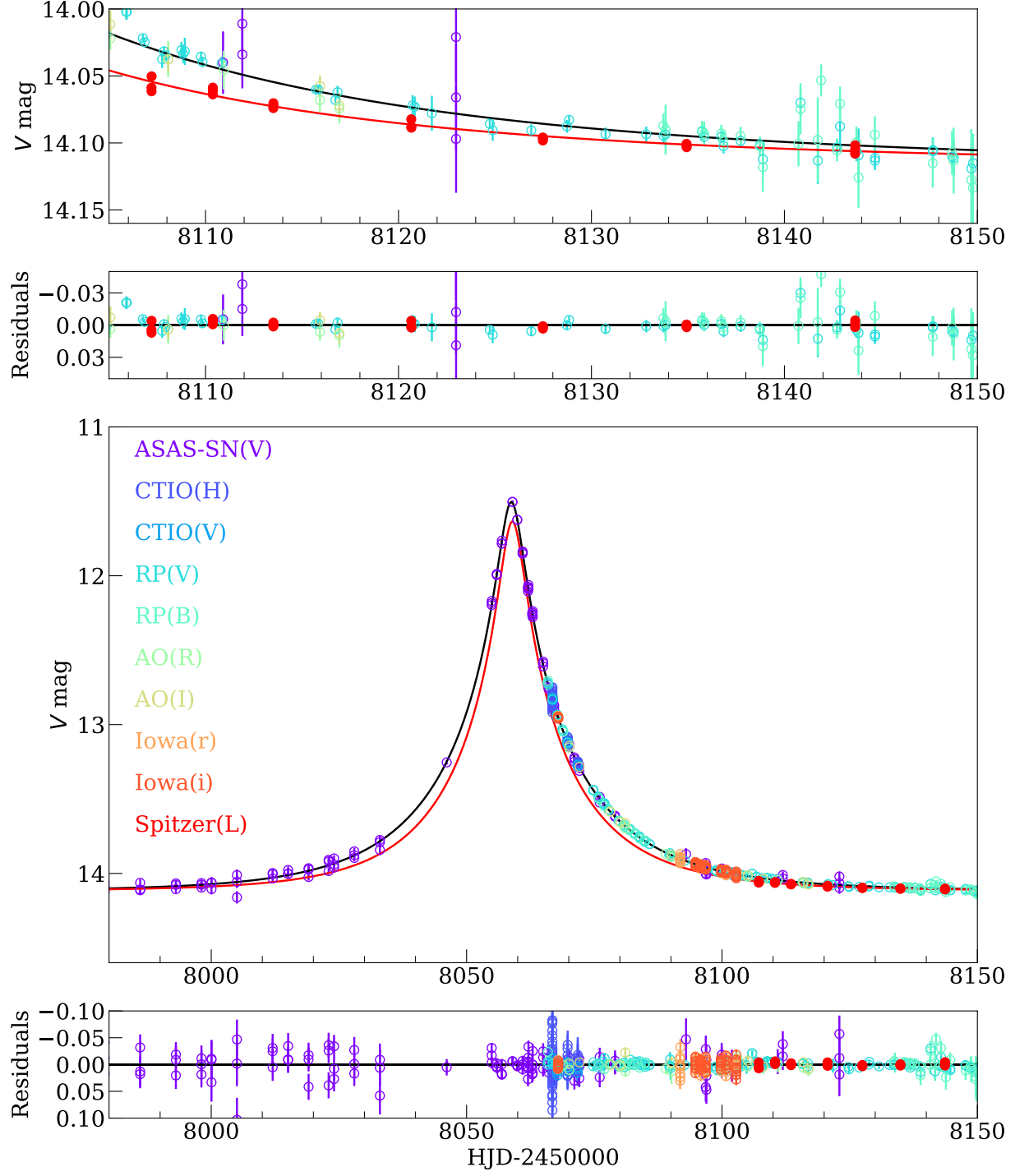


Figure 1. The light curves and data points of TCP J0507+2447. The upper panel show a close-up of *Spitzer* data points. The black line represent the best-fit $u_{0,\oplus} > 0$ with lens light model for the ground data, and the red line shows the corresponding model for *Spitzer*. The circles with different colors are ground-based data points from different telescopes or bands. The red dots are *Spitzer* data points.

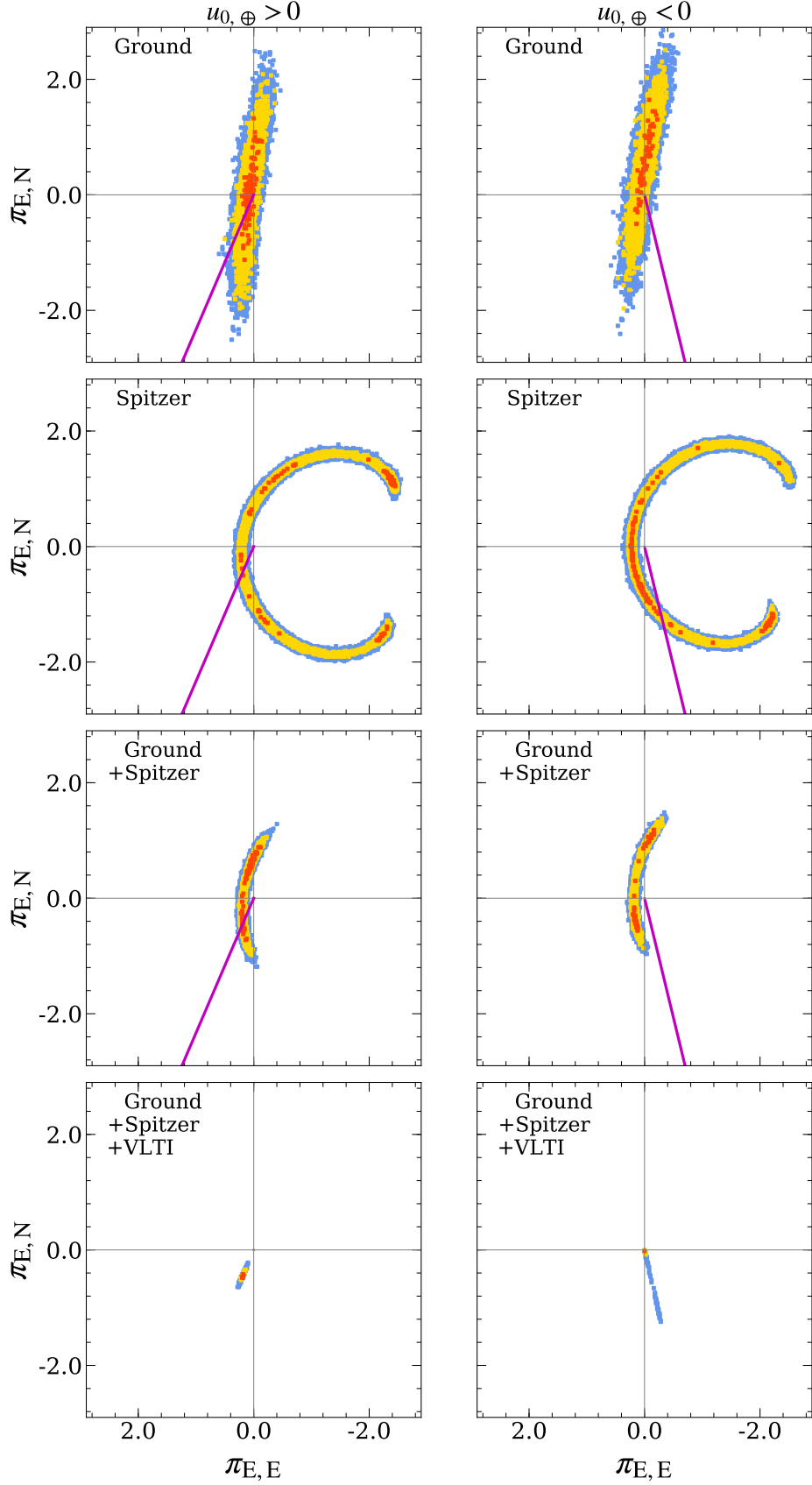


Figure 2. Likelihood distributions for π_E derived from MCMC. The left and right panels show the distributions for $u_0 > 0$ and $u_0 < 0$ solutions, respectively. Red, yellow, and blue show likelihood ratios $[-2\Delta \ln \mathcal{L}/\mathcal{L}_{\max}] < (1, 4, \infty)$, respectively. The magenta lines represent the best value of the VLTI directions.

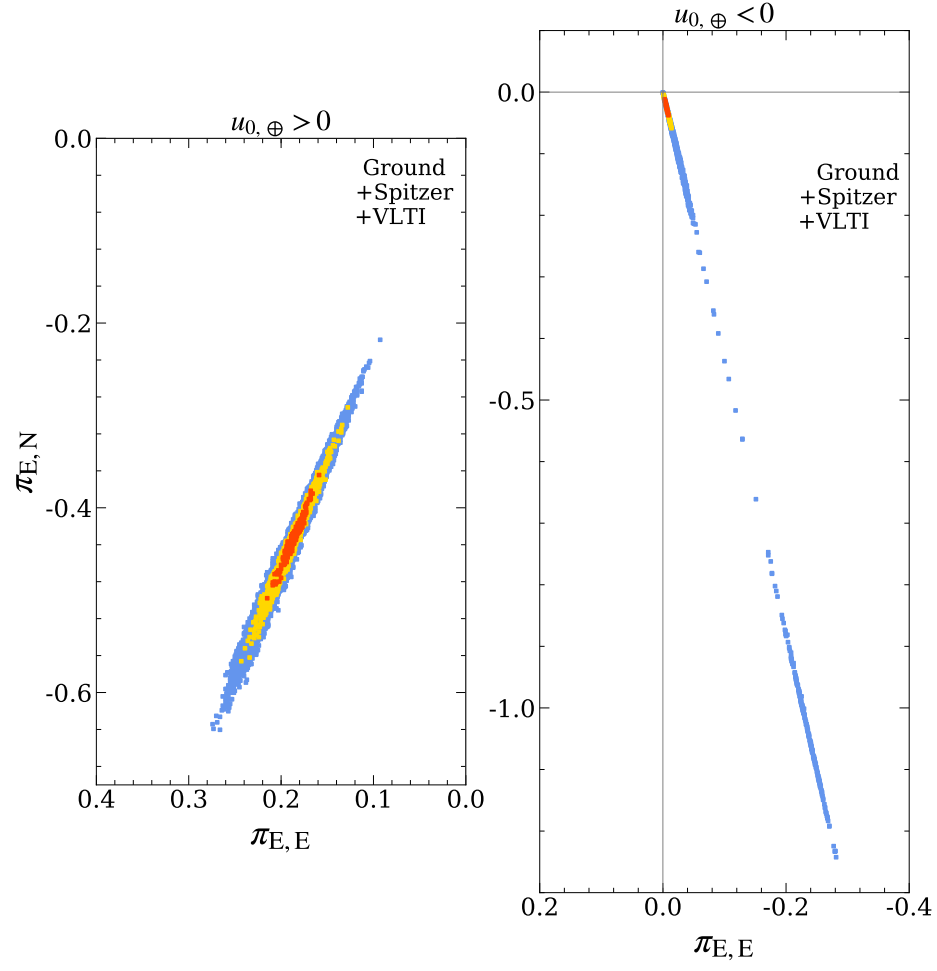


Figure 3. The Close-up of π_E Likelihood distributions with Ground + *Spitzer* + VLTI constraints. The symbols are similar to those in Figure 2.